Research Article

G.R. Kress* and D.T. Filipovic

An analytical nonlinear morphing model for corrugated laminates

https://doi.org/10.1515/cls-2019-0005
Received Oct 04, 2018; accepted Nov 07, 2018

Abstract: This paper contributes an analytical nonlinear morphing model for high-amplitude corrugated thin-walled laminates of arbitrary stack-up with a corrugation shape composed of circular sections. The model describes large deformations, the nonlinear relation between line force and global stretch, and the distribution of local line loads. The quarter-unit-cell approach together with assuming small material strains and a plane strain situation contribute to the model's simplicity. It is explained how the solution procedure minimizes the force and moment residual of the equilibrium of cutting and reaction line loads by using Newton's optimization method. Deformation results are verified by comparison with FEM simulation. The effects of laminate design and corrugation amplitude on deformations, line-force-stretch diagrams, and bending-curvature-stretch diagrams are presented and discussed.

Keywords: corrugated laminate; composite materials; large deformations; morphing

1 Introduction

Corrugated structural elements were first introduced in the construction sector by Henry Robinson Palmer in 1829 [1]. Later, the potential of corrugated sheets was employed in the aerospace industry. For instance, Hugo Junkers started to apply corrugated elements for the stabilization of wing and fuselage skins [2–5] as for the aircraft Ju-52 [1]. Since a few years ago, corrugated laminates made from fiber-reinforced composite materials are considered as candidate solutions for the flexible skins needed in morphing-wing design, and receive much research attention.

1.1 Corrugated laminates for morphing wings

Current modern wing design uses slats, flaps, and ailerons to adapt airfoil shape to the various starting, cruising, and landing flight situations. The movable structures for controlling flight are connected to the main wing structure by gearing mechanisms and, often hydraulic, actuation members. As wing-shape adaptation relies on relative rigid-body motion of the shape-control structures, gaps of changing size can not be avoided to disrupt the airfoil. The additional disadvantages of structural complexity and weight motivates the search for different methods of shape adaptation, where discrete movable structures are not needed and the main wing changes shape instead, which concept is named the morphing wing. Friswell [6] gives a critical review on the morphing-wing concept.
Review articles on morphing wing design with flexible skins made form corrugated laminates have been published by Thill *et al.* in 2007 [7], Barbarino *et al.* in 2011 [8], and Dayyani *et al.* in 2015 [9]. The most recent overview is provided in a book chapter by Airoldi *et al.* [10]. It is well accepted that the ideal flex-skin would be highly anisotropic, having a low in-plane axial stiffness but a high out-of-plane flexural stiffness [11].

1.2 Design, structural response and experiments

Yokozeki *et al.* [12] consider corrugated laminates for morphing wings, perform mechanical testing to measure stiffness values in various directions, and consider measures to maintain a smooth airfoil surface. Shaw *et al.* [13] perform optimization on the parameters of corrugations whose shapes are composed of straight sections to improve buckling strength. Takahashi *et al.* [14] describe the development of variable-camber morphing wing, which is mainly composed of corrugated structures. A prototype

***Corresponding Author: G.R. Kress:** Laboratory of Composite Materials and Adaptive Structures, Department of Mechanical and Process Engineering, ETH Zürich, Tannenstr. 3, CH-8092 Zürich, Switzerland; Email: gkress@ethz.ch
D.T. Filipovic: Laboratory of Composite Materials and Adaptive Structures, Department of Mechanical and Process Engineering, ETH Zürich, Tannenstr. 3, CH-8092 Zürich, Switzerland

model is designed by structural and aerodynamic analysis, manufactured, and tested in a wind tunnel. Previtali *et al.* [15] optimize a compliant morphing wing featuring a doubly corrugated flexible skin, manufacture a demonstrator and test its aeroelastic performance. Zheng and Qiu [16] propose an analytical method for finding critical buckling loads of composite corrugated plates which is treated as a substitute flat plate. The predictions consider laminate design variations and are compared with those made by detailed finite-element modeling. Kress and Thurnherr [17] investigate the response of laminates with high-amplitude circular-sections corrugation shapes to uniform pressure and find that the extreme anisotropy in bending stiffness invites global shear deformation to have a significant influence. Bai *et al.* [18] propose and study a corrugated flexible composite skin constructed with two thin-walled curved fibre-reinforced-plastics composite shells bonded together. They simulate the structural behavior and validate the simulation results with experiments.

1.3 Substitute-plate modeling

As early as 1986, Briassoulis [19] reviews analytical expressions for equivalent stiffnesses of orthotropic thin shells given in the literature to analyze corrugated shells based on the assumption that these can be presented as thin, equivalent orthotropic shells of uniform thickness. He also derives new expressions with improved mapping of equivalent properties. Yokozeki *et al.* [12] bases a simple analytical model on beam theory to predict stiffness along the corrugated direction of laminates made from woven composites which is considered a homogeneous material. Kress and Winkler [20] use thin-shell theory together with a unit-cell approach and the generalized plane-strain assumption with respect to the direction transverse to the corrugations to derive exact solutions for deformations and state variables valid for symmetric cross-ply laminates, where the corrugation shape is composed of circular sections. Kress and Winkler [21] derive a finite-element formulation based on the same assumption of generalized plane strain that reduces the number of independent spatial variables from three down to two. The finite-element mesh is subject to the periodicity conditions of the unit-cell approach. The model can simulate the behavior of any corrugation shape, maps any laminate design correctly, and captures all through-thickness effects which is in contrast to the limitations of thin-shell theory. Both of their models produce a substitute-plate ABD matrix. Xia *et al.* [22, 23] suggest an homogenization-based analytical model, which can be used for any corrugation shape. The base-sheet laminate ABD matrix must be free of couplings between extension and bending, extension and shear, as well as bending and torsion. Park *et al.* [24] present an analytical homogenization model for corrugated composite laminates that can be applied to any corrugation geometry. They give explicit expressions to calculate not only the effective extensional and bending stiffness but also the effective transverse shear stiffness for a composite corrugated panel. Nguyen-Minh *et al.* perform static [25] and vibration [26] analyses for which they develop homogenization models and cell-based smoothed Mindlin plate elements. They use their new methods to analyze trapezoidal and sinusoidally corrugated panels. The various models that have in common that they can calculate substitute-plate properties predict high compliance along the corrugated directions but are restricted to small deformations.

1.4 Stresses in corrugated laminates

Using the reduced finite-element approach by Kress and Winkler [21], Thurnherr *et al.* [27] present a parameter study on the influence of corrugation amplitude and different lay-ups on interlaminar stresses where they consider two geometries, one consists of circular sections and the other is a sinusoidal shape. They derive favorable configurations to minimize normalized interlaminar stresses.

1.5 Deformation limits of corrugated laminates

Winkler and Kress [28] determine the maximal possible deformations of a corrugated sheet where the corrugation pattern consists of two circular segments. The influence of the lay-up of cross-ply laminates and the influence of the geometry is investigated. The calculations are based on considerations of layer-wise strains that are calculated with the help of an analytical singly-curved shell model. For the evaluation of the influence of geometric nonlinearities finite element simulations are performed and compared to the linear strain limit calculations. The influence of scalable geometry parameters is also investigated. Schmitz and Horst [29] investigate deformation limits of circular corrugated unidirectional reinforced composites for bending dominated applications. They use a two-dimensional analytical stress-function approach that takes through-thickness normal stresses into account. Possible failure modes, namely fiber fracture and layer delamination, of unidirectional laminated corrugated sheets are predicted.

1.6 Large deformation of corrugated laminates

It is the direction along the corrugation where large deformations can appear if the corrugation amplitude is high enough. Thurnherr *et al.* [30] perform structural simulations with experimental validation to better understand the non-linear structural response. They also develop a simplistic non-linear model based on rods and rotational springs to efficiently simulate the highly non-linear load-displacement curves of corrugated laminates with high accuracy. However, the highly abstracted rod model maps neither the actual geometry nor the stresses within the laminate. Ren *et al.* [31] present a nonlinear planar beam formulation with stretch and shear deformations to study equilibria of a beam under arbitrary end forces and moments. The slope angle and stretch of the centroid line, and shear strain of cross-sections, are chosen as dependent variables in this formulation, and end forces and moments can be either prescribed or result from essential boundary conditions. For thin beams, where shear-strain influence on deformation is negligible, Kress and Winkler [32] use the same modeling idea some years earlier in context of finding realistic honeycomb-wall shapes resulting from the expansion process. This approach is used to develop the model for describing highly non-linear morphing deformations in the present work.

1.7 Structure of present work

Section 2 introduces geometric and mechanical unit cells and the geometric description of the assumed corrugation pattern consisting of circular sections as the reference configuration. The geometry description immediately yields the morphing stretch limits for very thin laminates. Section 2.3 explains how the assumption of cylindrical bending reduces the complexity of the relations between line loads and shell deformations as provided by the classical theory of laminated plates described in the text book by Jones [33]; however, the assumptions pose no restriction on laminate design. Section 2.4 explains the equilibrium conditions at the mechanical unit cell, how the external forces are equilibrated by cutting-line-load distributions, and how these determine mid-plane-strain and bending-curvature distributions of the laminate. Section 2.5 explains how the deformed configurations are found by integrating bending curvature to find cross-sectional rotation and by integrating cross-sectional rotations to find the positions of the deformed material points [32]. Also, the effect of mid-plane strain on deformed configurations is taken into account by integration [31]. Section 3 explains the numerical procedure for finding deformed configurations where the cutting line loads are compatible with the bending curvatures and mid-plane strains. Verified prediction of deformations and other results are found in Section 4 whereas Section 5 provides a critical discussion. Conclusions are placed in Section 6.

2 Theory

The theory holds for corrugated laminates where the reference configuration is a periodic corrugation pattern consisting of circular sections and where the laminates are much thinner than the circular-sections radii. Thus, the deformations are nonlinear whereas the material strains remain small [31, 32].

2.1 Geometric and mechanical unit cells

The sketch to the left in Figure 1 shows one periodic unit cell of the corrugation pattern and indicates the natural and essential boundary conditions. At all points marked

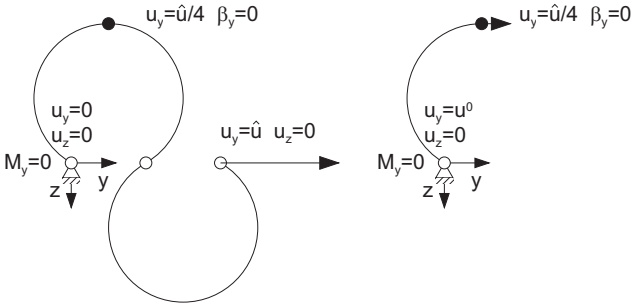

Figure 1: Geometric and mechanical unit cells

with open circles the bending moment M_y vanishes. The leftmost point is fixed in space but allowed to rotate. The point at the right of the geometric unit cell does not move along z, $u_z = 0$, and a specified displacement $u_y = \hat{u}$ imposes morphing strain. The geometric-unit-cell is point symmetric with respect to its center point, and the two circular segments are in themselves symmetric with respect to vertical lines. Therefore, the point marked with a solid circle cannot rotate. Because of these circumstances, and even though the stack-up sequence of the first circular section, say $[0_n/90_m]$, is reversed in the second one, the structural behavior of the geometric unit cell is fully described by the mechanical unit cell shown in the sketch to the right

of the figure. The relation between line loads and deformations is described in the local system xst shown in Figure 2, where the mapping between the coordinates of the moving trihedral $x\ \xi_2\ \xi_3$ and those of the reference coordinates is given with

$$\begin{Bmatrix} x \\ \xi_2 \\ \xi_3 \end{Bmatrix} = \begin{bmatrix} 1 & 0 & 0 \\ 0 & cos\theta & sin\theta \\ 0 & -sin\theta & cos\theta \end{bmatrix} \begin{Bmatrix} x \\ y \\ z \end{Bmatrix} . \tag{1}$$

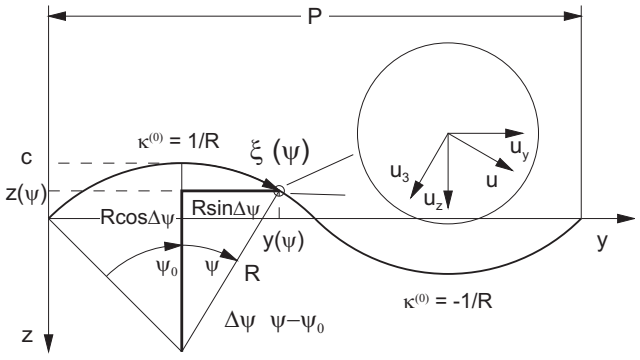

Figure 2: Unit-cell geometry and coordinate conventions

2.2 Reference configuration

Figure 2 indicates points in the reference configuration,

$$\begin{aligned} y^{(0)}(\xi_2) &= Rsin\Delta\psi \\ z^{(0)}(\xi_2) &= R\,[1 - cos\Delta\psi] - c, \end{aligned} \tag{2}$$

where

$$\Delta\psi = \psi - \psi_0 = \frac{\xi_2}{R} - \psi_0 = \kappa^0\xi_2 - \psi_0\,, \tag{3}$$

where the angleψ_0 is a shape characteristic depending on the corrugation amplitude c:

$$\psi_0 = acos\left(1 - \frac{c}{R}\right) . \tag{4}$$

Specified periodic length P and corrugation amplitude c determine the mid-plane curvature radius R:

$$R = \frac{16c^2 + P^2}{32c} \tag{5}$$

where the condition that the reference configuration must not penetrate itself limits c to

$$0 \le c \le \frac{P - t + \sqrt{(P-t)^2 - \frac{P^2}{4}}}{2}\,, \tag{6}$$

where t is laminate thickness. The reference-shape curvature $\kappa^{(0)}$ is the inverse of the radius R and Figure 3 illustrates the dependence of the shape curvature on the corrugation amplitude, where both quantities are normalized with respect to the periodic length P. Note that extreme morphing stretches, where the corrugated laminate tends to become flat, will create less bending curvatures for high-amplitude corrugations than for corrugation shapes composed of semi-circles ($\overline{c} = 0.25$). Point B in the reference configuration shown in Figure 5 is given with:

$$y_B^{(0)} = \frac{P}{4}\,; \qquad z_B^{(0)} = -c\,. \tag{7}$$

The mid-surface length of the mechanical unit cell L_s,

$$L_s = \psi_0\, R\,, \tag{8}$$

determines the morphing stretch limits shown in Figure 4:

$$\lambda = \frac{4L_s}{P}\,. \tag{9}$$

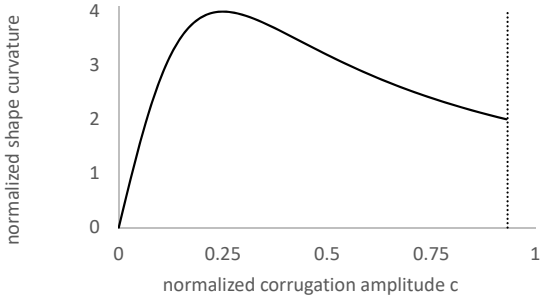

Figure 3: Normalized shape curvature $\overline{\kappa}^{(0)}$ versus normalized corrugation amplitude $\overline{c}$

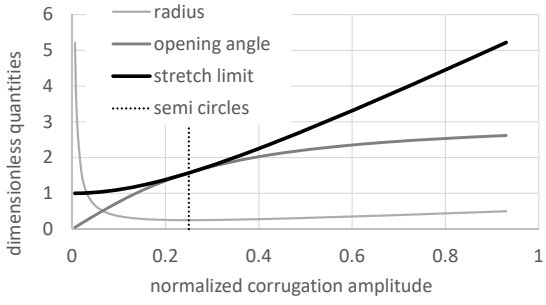

Figure 4: Morphing-stretch limits

2.3 Cylindrical bending and constitutive equations

Cylindrical bending implies that curvature deformations vanish, $\varepsilon_x^1 = \varepsilon_{xs}^1 = 0$. We also assume that the mid-plane strain transverse to the corrugations and the shearing strain vanish, $\varepsilon_x^0 = \varepsilon_{xs}^0 = 0$. As the laminate is free of couplings between between in-plane shear and direct line forces or twist and bending moments, $\varepsilon_{xs}^1 = 0$. The remaining relations between line loads and laminate deformations are:

$$\begin{aligned} N_x &= A_{12}\varepsilon_s^0 \\ N_s &= A_{22}\varepsilon_s^0 + B_{22}\varepsilon_s^1 \\ M_x &= D_{12}\varepsilon_s^1 \\ M_s &= B_{22}\varepsilon_s^0 + D_{22}\varepsilon_s^1 \end{aligned} \tag{10}$$

2.4 Mechanical unit-cell equilibrium

Figure 5 redraws the mechanical unit cell identified in Figure 1, where θ coincides with $\Delta\varphi$ if no deformation is applied, and indicates line loads reacting to the essential boundary conditions. A specified line force $N_B = N_y = N$ causes the reaction line force $N_A = -N$ at point A. The internal moment at B is obtained from the cross product of the reaction N_A and distance between the line along which N_A acts and point B:

$$\begin{Bmatrix} 0 \\ 0 \\ z_B \end{Bmatrix} \times \begin{Bmatrix} 0 \\ -N \\ 0 \end{Bmatrix} = \begin{Bmatrix} z_B N \\ 0 \\ 0 \end{Bmatrix} = \begin{Bmatrix} M_B \\ 0 \\ 0 \end{Bmatrix} \tag{11}$$

The local mid-surface in-plane line force $N_2(\xi_2)$ along ξ_2

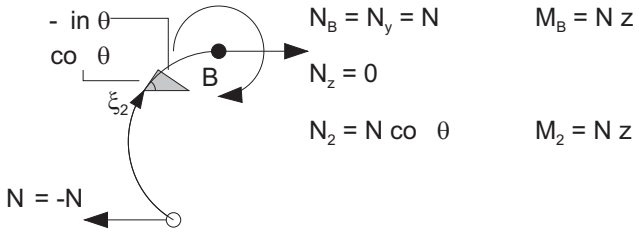

Figure 5: Equilibrium at unit cell and internal line loads

is a component of N obtained from the transformation rule (1),

$$N_2(\xi_2) = N\cos(\theta)\,, \tag{12}$$

whereas the local transverse force $Q_3(\xi_2)$ is not considered as the laminate thickness is assumed much smaller than the corrugation-shape curvature. We connect the local line loads with the second and the fourth of the laminate constitutive equations in (2) to obtain:

$$\begin{Bmatrix} N\cos(\theta) \\ Nz \end{Bmatrix} = \begin{bmatrix} A_{22} & B_{22} \\ B_{22} & D_{22} \end{bmatrix} \begin{Bmatrix} \varepsilon_2^0 \\ \varepsilon_2^1 \end{Bmatrix}. \tag{13}$$

Resolving (13) for the laminate deformations gives:

$$\begin{Bmatrix} \varepsilon_2^0 \\ \varepsilon_2^1 \end{Bmatrix} = \frac{1}{D} \begin{bmatrix} D_{22} & -B_{22} \\ -B_{22} & A_{22} \end{bmatrix} \begin{Bmatrix} N\cos(\theta) \\ Nz \end{Bmatrix}, \tag{14}$$

where D is the determinant:

$$D = A_{22}D_{22} - B_{22}^2\,. \tag{15}$$

2.5 Curvature and rotation

The curvature $\kappa^{(t)}(\xi_2)$ of the deformed configuration is the sum of the shape curvature of the reference configuration $\kappa^{(0)} = 1/R$ and of the bending curvature $\varepsilon_2^1(\xi_2)$ due to deformation caused by mechanical load (14):

$$\kappa^{(t)}(\xi_2) = \kappa^{(0)} + \varepsilon_2^1(\xi_2)\,, \tag{16}$$

where the linear distribution of the bending moment M_2, and with it that of $\varepsilon_2^1(\xi_2)$, along z has been considered. The total slope follows from integrating the curvature along the curvilinear coordinate ξ_2 [31, 32]:

$$\theta^{(t)}(\xi_2) = \int_0^{\xi_2} \kappa^{(t)}(\sigma)\,d\sigma + C_1 \tag{17}$$

where the integration constant C_1 must be adjusted to maintain the symmetry condition at B, namely $\theta_B^{(t)} = 0$. The total slope equals the angle of rotation in the directional transformation (1).

2.6 Deformed configuration

The deformed configuration is calculated from integrating mid-plane strain ε_2^0 and rotation θ over the curved length ξ_2.

2.6.1 Stretch of line elements

A reference-configuration line element of the mid-surface $d\xi_2^{(0)}$ changes length by the stretch λ:

$$d\xi_2^{(t)} = \lambda d\xi_2^{(0)} = \left(1 + \varepsilon_2^0\right) d\xi_2^{(0)}\,. \tag{18}$$

At position ξ_2 the stretching of the line element gives the incremental displacements [31]:

$$du_y^0 = cos(\theta)\,\varepsilon_2^0\,d\xi_2^{(0)}\,; \quad du_z^0 = -sin(\theta)\,\varepsilon_2^0\,d\xi_2^{(0)}\,. \tag{19}$$

Note that the stretch of the line elements becomes significant at the end of morphing action when the corrugated laminate has become almost flat. In addition, typical carbon-fiber reinforced material may fail at less than 0.5 percent strain transverse to the fiber direction.

2.6.2 Integration of the rotation

Positions of points in the deformed configuration are found by integrating the slope [32] and thereby considering the stretch [31] of line elements:

$$du_y = du_y^0 + du_y^1\,; \quad du_z = du_z^0 + du_z^1\,. \tag{20}$$

At position ξ_2 the stretching of the line element gives the incremental displacements:

$$y^{(t)}(\xi_2) = \int_0^{\xi_2} \cos(\theta)\,\lambda d\sigma \tag{21}$$

$$z^{(t)}(\xi_2) = -\int_0^{\xi_2} \sin(\theta)\,\lambda d\sigma\,.$$

At the reference configuration the point B indicated in Figure 5 has the position $y_B^{(0)} = P/4$, $z_B^{(0)} = -c$. Deformation changes that position to:

$$y_B^{(t)} = \int_0^{L_s} \cos(\theta)\,\lambda d\sigma \tag{22}$$

$$z_B^{(t)} = -\int_0^{L_s} \sin(\theta)\,\lambda d\sigma\,.$$

2.6.3 Displacements in reference coordinates

Displacements follow from the difference between current and reference configurations:

$$u_y = y^{(t)} - y^{(0)}\,; \quad u_z = z^{(t)} - z^{(0)}\,, \tag{23}$$

which yields:

$$u_y(\xi_2) = \int_0^{\xi_2} \cos(\theta)\,\lambda d\sigma - y^{(0)} \tag{24}$$

$$u_z(\xi_2) = -\int_0^{\xi_2} \sin(\theta)\,\lambda d\sigma - z^{(0)}\,.$$

3 Solution algorithm

Deformed configurations of the problem at hand depend most directly on an applied line force N. On the other hand, it is desired to specify morphing stretch. The solution algorithm is therefore partitioned into outer and inner iterative processes, where the outer process finds the line force effectuating that the actual stretch is equal to the specified one, and where the inner loop finds a deformed configuration where the reacting line loads agree with the internal line loads equilibrating the external force. Creating stretch-force diagrams from zero up to the specified stretch $\hat{\lambda}$ are also desired; therefore the line force N is increased in steps and the deformed deformations are calculated by the inner process until the actual stretch comes close to or exceeds the specified stretch. Then, the outer process starts to minimize the difference between actual and specified stretches.

3.1 Inner process

A loop on load steps creates the data points for line-force-displacement diagrams, as Figure 6 shows. The procedure starts with applying the force N to the reference configuration $y^{(0)}(\xi_2)$ and $z^{(0)}(\xi_2)$ to calculate curvature and mid-plane strain after (14), angles after (17), and the deformed configuration after (21). At this point, the deformed configuration's interior loads cannot be in equilibrium with the

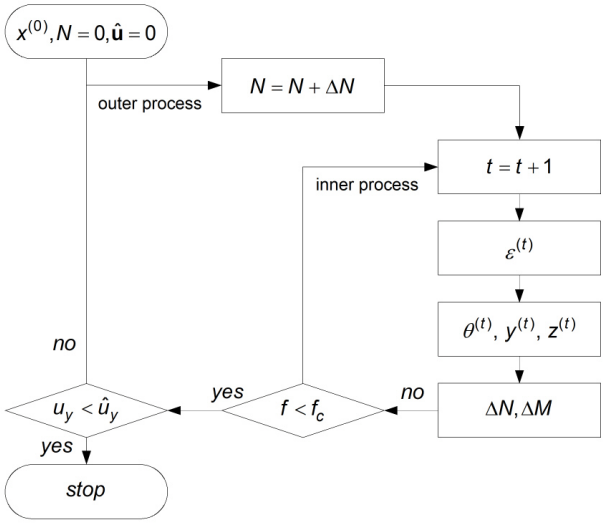

Figure 6: Solution scheme

external forces. A scalar error measure is provided with:

$$f = \int_0^{L_s} \begin{Bmatrix} \Delta N_2 \\ \Delta M_2 \end{Bmatrix}^T \begin{Bmatrix} \Delta N_2 \\ \Delta M_2 \end{Bmatrix} ds\,, \tag{25}$$

where the symbol s replaces ξ_2 and where

$$\begin{Bmatrix} \Delta N_2 \\ \Delta M_2 \end{Bmatrix} = \begin{Bmatrix} N_2^{int} \\ M_2^{int} \end{Bmatrix} - \begin{Bmatrix} N_2^{ext} \\ M_2^{ext} \end{Bmatrix}\,, \tag{26}$$

where the first term in the parentheses presents interior loads corresponding with the actual deformation

$$\begin{Bmatrix} N_2^{int} \\ M_2^{int} \end{Bmatrix} = \begin{bmatrix} A_{22} & B_{22} \\ B_{22} & D_{22} \end{bmatrix} \begin{Bmatrix} \varepsilon_2^0 \\ \varepsilon_2^1 \end{Bmatrix} \tag{27}$$

and the second term contains the exterior loads dictated by global equilibrium. In a numerical presentation of the problem the integral becomes a sum over all entries of the data-point arrays:

$$f = \sum_{k=1}^{n+1} f_k = \sum_{k=1}^{n+1} \begin{Bmatrix} \Delta N_2 \\ \Delta M_2 \end{Bmatrix}_k^T \begin{Bmatrix} \Delta N_2 \\ \Delta M_2 \end{Bmatrix}_k \Delta s \tag{28}$$

where the curved mid-plane length L_s is subdivided into n sections of equal length Δs and the state variables are assigned to the $n+1$ interface and end points. The plate deformations $\varepsilon_{2_k}^0$ and $\varepsilon_{2_k}^1$ completely control the deformed configuration and are therefore solution parameters of the quadratic error-function f. The Newton method minimizes the error function f,

$$\boldsymbol{\varepsilon}_k^{(t+1)} = \boldsymbol{\varepsilon}_k^{(t)} + \Delta\boldsymbol{\varepsilon}_k^{(t)}\,, \tag{29}$$

where the array $\boldsymbol{\varepsilon}_k$ contains midplane strain and bending curvature and where the improvement $\Delta x^{(t)}$ is:

$$\boldsymbol{\varepsilon}_k^{(t)} = \begin{Bmatrix} \varepsilon_2^0 \\ \varepsilon_2^1 \end{Bmatrix}_k^{(t)}, \quad \Delta\boldsymbol{\varepsilon}_k^{(t)} = -\left(\nabla\nabla f\right)^{-1} \nabla f_k^{(t)}\,. \tag{30}$$

The derivatives can be calculated analytically, namely the gradient $\nabla f_k^{(t)}$

$$\nabla f_k^{(t)} = 2 \begin{Bmatrix} \Delta N_2 \\ \Delta M_2 \end{Bmatrix}_k^{(t)^T} \begin{bmatrix} A_{22} & B_{22} \\ B_{22} & D_{22} \end{bmatrix} ds\,, \tag{31}$$

and the Hesse matrix $\nabla\nabla f^{(t)}$:

$$\nabla\nabla f_k = 2 \begin{bmatrix} A_{22} & B_{22} \\ B_{22} & D_{22} \end{bmatrix}^T \begin{bmatrix} A_{22} & B_{22} \\ B_{22} & D_{22} \end{bmatrix} ds\,. \tag{32}$$

The increments $\Delta\boldsymbol{\varepsilon}_k^{(t)}$ of mid-plane strain and curvature are:

$$\Delta\boldsymbol{\varepsilon}_k^{(t)} = -\boldsymbol{\varepsilon}_k^{(t)} - \frac{1}{D} \begin{bmatrix} D_{22} & -B_{22} \\ -B_{22} & A_{22} \end{bmatrix} \begin{Bmatrix} N_2^{ext} \\ M_2^{ext} \end{Bmatrix}_k^{(t)}, \tag{33}$$

so that the Newton Method gives the up-date rule:

$$\boldsymbol{\varepsilon}_k^{(t+1)} = -\frac{1}{D} \begin{bmatrix} D_{22} & -B_{22} \\ -B_{22} & A_{22} \end{bmatrix} \begin{Bmatrix} N_2^{ext} \\ M_2^{ext} \end{Bmatrix}_k^{(t)}. \tag{34}$$

As the line loads equilibrating external loading depend on deformations, the up-date must be improved in iterations. We find rapid convergence of this procedure up to intermediate stretch values, or deformations, above which the procedure tends to diverge. This phenomenon is generally caused by the objective function deviating too far away from a quadratic polynomial so that the minimum-point estimates of the Newton method become erroneous. The problem is mitigated by the modified Newton method employing line searches:

$$\boldsymbol{\varepsilon}_k^{(t+1)} = \boldsymbol{\varepsilon}_k^{(t)} + \alpha\Delta\boldsymbol{\varepsilon}_k^{(t)} \tag{35}$$

where α is the step length minimizing f along the search direction $\Delta\boldsymbol{\varepsilon}_k^{(t)}$. We also find that simply multiplying the changes $\Delta\boldsymbol{\varepsilon}_k^{(t)}$ as predicted by (30) with a damping factor μ,

$$\mu = k^p \qquad p = -\frac{1}{4}\,, \tag{36}$$

where k is inner-process iteration number, preserves convergence for any specified displacement.

3.2 Outer process

In order to let the actual deformed length $y_B^{(k)}$ converge against the specified value $\hat{y}_B$, we use the interval section method which is based on the rule of proportion:

$$N^{(k+1)} = N^{(k-1)} + \left(N^{(k)} - N^{(k-1)}\right) \frac{\left(\hat{y}_B - y_B^{(k-1)}\right)}{\left(y_B^{(k)} - y_B^{(k-1)}\right)} \tag{37}$$

The updated length $y_B^{(k+1)}$ should be closer to the specified stretch than the previous values:

$$\left|\Delta y_B(N^{(k+1)})\right| < \min\left(\left|\Delta y_B^{(k-1)}\right|, \left|\Delta y_B^{(k)}\right|\right)\,, \tag{38}$$

where

$$\Delta y_B(N^{(k+1)}) = y_B(N^{(k+1)}) - \hat{y}_B\,; \quad \Delta y_B^{(k)} = y_B^{(k)} - \hat{y}_B\,. \tag{39}$$

If condition (38) applies, the line force N^{k+1} replaces either N^k or N^{k-1} depending on which of the two leads to greater deviation of the actual stretch away from its specified value.

$$\Delta y_B^{(k-1)} > \Delta y_B^{(k)} \begin{cases} \text{true} & \rightarrow N^{(k-1)} = N^{(k+1)} \\ \text{false} & \rightarrow N^{(k)} = N^{(k+1)} \end{cases} \tag{40}$$

4 Stress evaluation

It is assumed that the ratio between laminate thickness and curvature is small enough for strains and stresses to be linear through laminate thickness. Stresses depend on mechanical as well as thermal-hygral loads. Thermal-hygral loads are taken into account by the equivalent line loads reacting to a full constraint of the free strains $\boldsymbol{\varepsilon}^{free}$ [33]:

$$\mathbf{N}^{eqv} = -\sum_{k=1}^{N} \overline{\mathbf{Q}}\,\boldsymbol{\varepsilon}^{free}\,(z_k - z_{k-1}) \tag{41}$$

$$\mathbf{M}^{eqv} = -\frac{1}{2}\sum_{k=1}^{N} \overline{\mathbf{Q}}\,\boldsymbol{\varepsilon}^{free}\left(z_k^2 - z_{k-1}^2\right)$$

where the free strains arise from changes of temperature ΔT and moisture content ΔH and the corresponding coefficients of expansion:

$$\boldsymbol{\varepsilon}^{free} = \boldsymbol{\alpha}\Delta T + \boldsymbol{\beta}\Delta H \tag{42}$$

Together with the mechanical lines loads, the equivalent line loads form the fictitious loads:

$$\begin{Bmatrix}\mathbf{N}\\ \mathbf{M}\end{Bmatrix}^{fict} = \begin{Bmatrix}\mathbf{N}\\ \mathbf{M}\end{Bmatrix}^{mech} - \begin{Bmatrix}\mathbf{N}\\ \mathbf{M}\end{Bmatrix}^{eqv} \tag{43}$$

If thermal-hygral deformations have contributed to what may be considered the reference-configuration shape $y^{(0)}, z^{(0)}$ in the sense that this is free of external mechanical loads, all schemes, modeling the effects of applying mechanical load on deformation, explained in Sections 2 and 3 as well as the deformation and structural responses shown in Section 4 remain valid by virtue of linear superposition that is justified under the small-strains assumption. For calculating strains and stresses; however, the thermal-hygral stresses must be taken in account with:

$$\begin{Bmatrix}\boldsymbol{\varepsilon}^0\\ \boldsymbol{\kappa}\end{Bmatrix} = \begin{bmatrix}\mathbf{A} & \mathbf{B}\\ \mathbf{B} & \mathbf{D}\end{bmatrix}^{-1} \begin{Bmatrix}\mathbf{N}\\ \mathbf{M}\end{Bmatrix}^{fict} \tag{44}$$

and

$$\boldsymbol{\sigma}(z) = \overline{Q}_k\left(\boldsymbol{\varepsilon}^0 + z\boldsymbol{\kappa} - \boldsymbol{\varepsilon}^{free}\right); \quad z_{k-1} \le z \le z_k \tag{45}$$

5 Simulations

5.1 Material, laminates, and reference shape

The sample problem uses unidirectional laminates made from prepregs T300/epoxy where Table 1 shows relevant material properties. The samples include a symmetric laminate [90] and an unsymmetric one $[90, 0_2]$, both of thickness $t = 1mm$. The laminates are formed into corrugations with periodic length $P = 100mm$ and amplitude $c = 93.3mm$.

Table 1: Relevant material properties of unidirectional T300/epoxy with fiber-volume fraction $v_f = 0.6$. Source: DORNIER SYSTEM GmbH

fiber	E_1	E_2	ν_{12}	α_1	α_2
	[MPa]		[–]	$[10^{-6}/K]$	
T 300	135000	10000	0.27	–0.6	30

5.2 Deformed configurations

Figure 7 shows plots of the deformed shapes under the specified displacements mentioned in the figure caption. It appears that the influence of laminate design increases at higher stretches where the line force gains significance if compared with the line moment. The strain-bending coupling of the unsymmetric laminate then causes higher deflections. For verifying the results of the analytical model, the deformations of the corrugated laminate with symmetric layup, as shown in Figure 7 have also been simulated by using a commercial FEM program [34], see Figure 8. The curved length of the quarter-unit-cell model is meshed with 100 two-dimensional finite elements with quadratic shape functions for mapping plain strain problems. Under a specified displacement at point B of $\hat{u}_y$ the FEM simulation yields a position $z_B = -8.54mm$ whereas the present analytical model evaluates $z_B = -8.48mm$. The relative

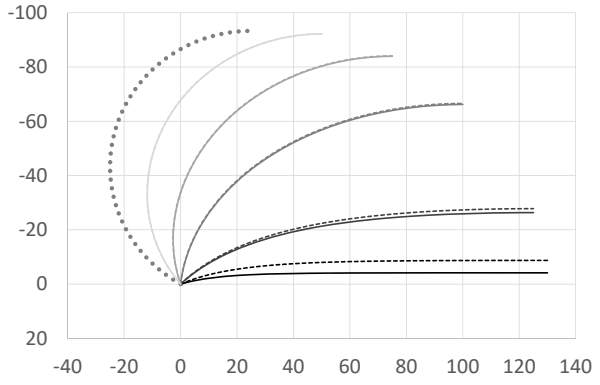

Figure 7: Reference and morphed shapes of corrugated laminates $[90, 0_2]$ (solid lines) and $[90_3]$ (dashed lines) with maximum corrugation amplitude; stretches: 2, 3, 4, 5, and 5.2.

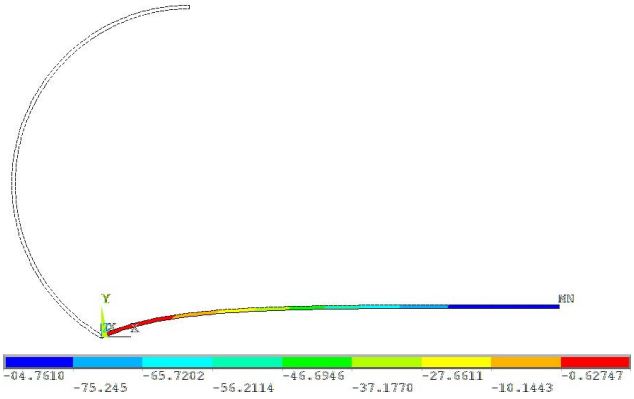

Figure 8: Deformed configuration for the symmetric laminate obtained with a commercial FEM program

deviation between the two displacements, where the FEM result is used as reference, is −0.7%. If the vertical displacement is considered rather than the position, the relative deviation is one order of magnitude smaller.

5.3 Stretch-line-force diagrams

The observation, that at higher stretches the line force gains a more significant role on the deformations, is corroborated with the knee-shape characteristic of global line-force-stretch diagrams shown in Figure 9 where the

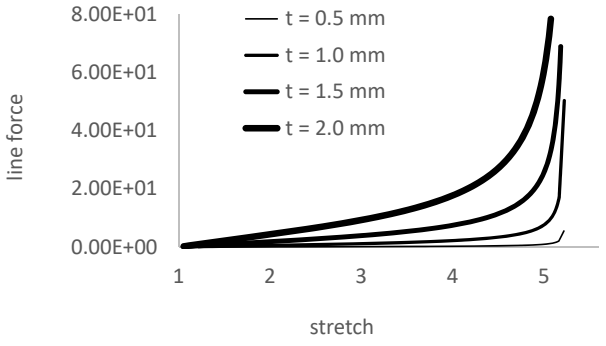

Figure 9: Influence of laminate thickness on force-stretch diagrams

knee-shape becomes more pronounced for thinner wall thickness. Figure 10 shows the influence of corrugation amplitude$c$ at the same thickness $t = 1mm$. The diagrams indicate that not only the stretch limits reduce quickly but also that the average force required to approach the respective stretch limits increase significantly with decreasing corrugation amplitude.

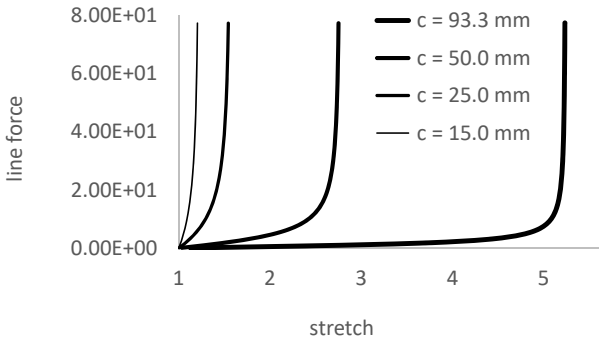

Figure 10: Influence of corrugation amplitude on force-stretch diagrams

5.4 Bending curvatures

Figure 11 illustrates the curvatures at point B during mor-

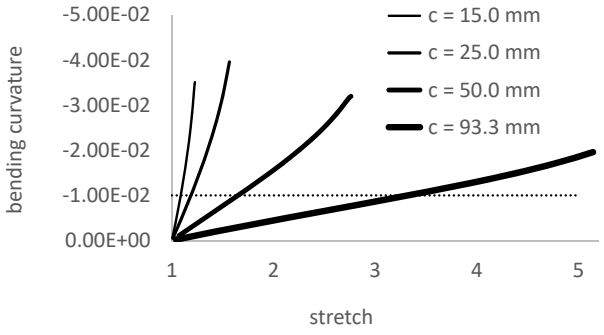

Figure 11: Bending curvatures versus corrugation amplitude, $t = 1mm$

phing action for the various corrugation amplitudes indicated in the figure legend. The distribution of the maximum bending curvatures is directly related to the dependence of shape curvature on corrugation amplitude, see Figure 3. The dotted line in Figure 11 indicates the curvature that leads to a maximum bending strain of $\varepsilon(z = \pm t/2) = \mp 0.5\%$. Obviously, bending strain scales linearly with laminate thickness so that thinner laminates suffer less material straining during morphing action, so that they endure higher stretches.

6 Discussion

It can be seen from Figure 7 that for the relatively moderate stretch value $\lambda = 2$ of a high-amplitude corrugated lami-

nate the displacement of material points towards the neutral plane of the corrugated laminate is small, so that the reduction of the cross-sectional bending moment of inertia remains small as well. Considering the potential application as a flexible part embedded in wing skin, the high-amplitude corrugated laminate could also play the role of a local wing-skin stiffener where the bending stiffness contribution remains unaffected within moderate morphing stretches. In addition to its mechanical advantages, the high-amplitude corrugation shape, where the laminate almost touches itself, causes less aerodynamic roughness than lower amplitudes [35], where the sketch of a wing skin with integrated flexible-skin section shown in Figure 12 gives a visual impression.

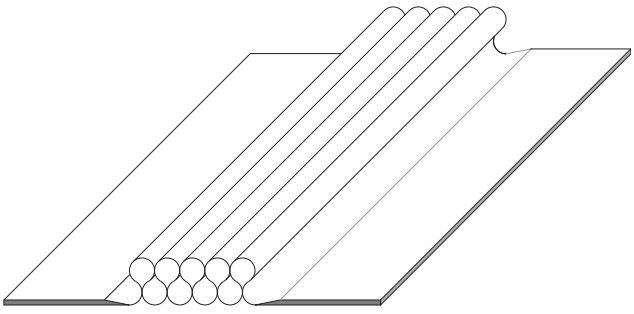

Figure 12: Long plate or shallow shell with flexible-skin section

Other advantages of the high-amplitude corrugated laminate consisting of circular segments is that bending curvature is smaller than for lower amplitudes or other corrugation shapes [30] and, by choosing thickness-to-shape-curvature ratios small enough, bending stresses can be kept below values critical for fatigue strength. Moreover, there is no need to fully utilize maximum morphing stretches of high-amplitude corrugated laminates: at stretch $\lambda = 2$ (corresponds with 100% structural strain of the flexible-skin section) the deformed shape retains much of the bending moment of inertia of the reference shape and actuation force as well as material strains remain small.

7 Conclusion

A nonlinear model for large deformation of cylindrical shells under cylindrical bending has been developed and applied to describe the morphing action of corrugated laminates where the reference configuration shape is composed of circular sections. The model allows instantaneously creating diagrams of structural response to applied stretch or force. The deformed configuration at specified stretch is verified through excellent agreement with the results of commercial FEM software modeling.

The model provides a very efficient design tool and has been used to show that large corrugation amplitudes offer high stretchability and that utilizing only a small part of it does not change the shape characteristics significantly so that the cross-sectional bending stiffness is maintained through such moderate stretching. All results indicate practical advantages of the high-amplitude corrugation shape consisting of circular sections over other corrugation shapes.

Acknowledgement: The authors gratefully acknowledge the support of the Swiss National Science Foundation (project no. 169468 and grant no. 200021_169468 / 1).

References

[1] Mornement, A., and Holloway S., Corrugated Iron - Builing on the Frontier, Francis Lincoln Limited, London, UK, 2007.
[2] H. Junkers, Flying-machine supporting surface, US Patent No. 14627, 1923.
[3] H. Junkers, Corrugated sheet metal, US Patent No. 1517633, 1924.
[4] H. Junkers, Flying-machine covering, US Patent No. 1553695, 1925.
[5] H. Junkers, Corrugated sheet-metal shape, US Patent No. 1704326, 1929.
[6] M.I. Friswell, Morphing aircraft: An improbable dream? in: Proceedings of the ASME Conference on Smart Materials, Adaptive Structures and Intelligent Systems SMASIS2014, Newport, Rhode Island, USA, 2014.
[7] Thill, C., J.A. Etches, I.P. Bond, K.D. Potter, and P.M. Weaver, Corrugated composite structures for aircraft morphing skin applications, in: (Ed.), 18th Int. Conf. of Adaptive Structures and Technologies, Vol. 134, Ottawa, Ontario, Canada, 2007, pp. 507–14.
[8] Barbarino, S., O. Bilgen, R.M. Ajaj, M.I. Friswell, D.J. Inman, A Review of Morphing Aircraft, J. Intell Mater Syst Struct 22 (9) (2011) 823–77.
[9] Dayyani, I., A.D. Shaw, E. Saavedra Flores, M.I. Friswell, The Mechanics of Composite Corrugated Structures: A Review with Applications in Morphing Aircraft, Composite Structures 133 (2015) 358–80.
[10] Airoldi, A., G. Sala, L.A. Di Landro, P. Bettini, A. Gilardelli, Composite Corrugated Laminates for Morphing Applications, in: Antonio Concilio, Ignazio Dimino, Leonardo Lecce, Rosario Pecora (Ed.), Morphing Wing Technologies, Butterworth and Heinemann, Oxford, 2018, Ch. 9, pp. 247–276.
[11] Gandhi, F., Anusonthi, P., Skin design studies for variable camber morphing airfoils, Smart Materials and Structures 17 (2008) 1–8.
[12] Yokozeki T., S.-I. Takeda, T. Ogasawara, T. Ishikawa, Mechanical properties of corrugated composites for candidate materials of flexible wing structures, Composites: Part A 37 (2006)

1578?1586.
[13] Shaw, A.D., I. Dayyani, M.I. Friswell, Optimisation of Composite Corrugated Skins for Buckling in Morphing Aircraft, Composite Structures 119 (2015) 227–237.
[14] Takahashi, H., T. Yokozeki and Y. Hirano, Development of Variable Camber Wing with Morphing Leading and Trailing Sections Using Corrugated Structures, Journal of Intelligent Material Systems 27 (20) (2016) 2827–2836.
[15] Previtali, F., G. Molinari, A. F. Arrieta, M. Guillaume and P. Ermanni, Design and Experimental Characterization of a Morphing Wing with Enhanced Corrugated Skin, Journal of Intelligent Material Systems 27 (2) (2016) 278–292.
[16] Zheng, Y., Z. Qiu, Analysis of the Critical Buckling Loads of Composite Corrugated Plates Under Nonlinearly Distributed Compressive Loads Accounting for Flexural Twist Coupling, Acta Mechanica 227 (2016) 3407–3428.
[17] Kress, G., C. Thurnherr, Bending Stiffness of Transversal Isotropic Materials, Composite Structures 176 (2017) 692–701.
[18] Bai, J.B., D. Chen, J.J. Xiong, R.A. Shenoi, A Corrugated Flexible Composite Skin for Morphing Applications, Composites Part B 131 (2017) 134–143.
[19] Briassoulis, D., Equivalent Orthotropic Properties of Corrugated Sheets, Computers and Structures 23 (2) (1986) 129–138.
[20] Kress, G., M. Winkler, Corrugated Laminate Homogenization Model, Composite Structures 92 (3) (2010) 795–810.
[21] Kress, G., M. Winkler, Corrugated Laminate Analysis: A Generalized Plane-Strain Problem , Composite Structures 93 (2011) 1493–1504.
[22] Xia, Y., M.I. Friswell, Equivalent Models of Corrugated Laminates for Morphing Skins, Active Passive Smart Struct Integr Syst 7977 (797711-79711-0).
[23] Xia, Y., Flores, E.I.S., M.I. Friswell, Equivalent Models of Corrugated Panels, Int J Solids Struct 49 (13) (2012) 1453–62.
[24] Park, K.-J., K. Jung, Y.-W. Kim, Evaluation of Homogenized Effective Properties for Corrugated Composite Panels, Composite Structures 140 (2016) 644–654.
[25] Nguyen-Minh, N., N. Tran-Van, T. Bui-Xuan, T. Nguyen-Thoi, Static Analysis of Corrugated Panels Using Homogenization Models and a Cell-Based Smoothed Mindlin Plate Element (CS-MIN3), Frontiers of Structural Civil Engineering https://doi.org/10.1007/s11709-017-0456-0.
[26] Nguyen-Minh, N., N. Tran-Van, T. Bui-Xuan, T. Nguyen-Thoi, Free Vibration Analysis of Corrugated Panels Using Homogenization Methods and a Cell-Based Smoothed Mindlin Plate Element (CS-MIN3), Thin-Walled Structures 124 (2018) 184–201.
[27] Thurnherr, C., L. Ruppen, G. Kress, P. Ermanni, Interlaminar Stresses in Corrigated Laminates, Composite Structures 140 (2016) 296–308.
[28] Winkler, M., G. Kress, Deformations limits for Corrugated Cross-Ply Laminates, Composite Structures 92 (6) (2010) 1458–68.
[29] A. Schmitz, P. Horst, Bending deformation limits of corrugated unidirectionally reinforced laminates, Composite Structures 107 (2014) 103–111.
[30] Thurnherr, C.N., L. Ruppen, G. Kress, P. Ermanni, Non-linear Striffness Response of Corrugated Laminates in Tensile Loading, Composites structures 157 (2016) 244–255.
[31] Ren, H., W.D. Zhu, W. Fan, A nonlinear planar beam formulation with stretch and shear deformations under end forces and moments, International Journal of Non-Linear Mechanics 85 (2016) 126–142.
[32] Kress, G.R., Winkler, M., Honeycomb Sandwich Residual Stress Deformation Pattern, Composite Structures 89 (2009) 294–302.
[33] Jones, R.M., Mechanics of Composite Materials, Hemisphere Publishing Corporation, New York, 1975.
[34] ANSYS® Academic Research, Release 18.2.
[35] C. Thill, J.D. Downsborough, S.J. Lai, I.P. Bond, D.P. Jones, Aerodynamic study of corrugated skins for morphing wing applications, Awronautical Journal 3407 (2010) 237–244.